# Synthesis of CsPbBr₃/ZIF-8 Pe-MOF composite: A fluorometric sensing probe for 4 – nitroaniline and rhodamine blue

Highlights

This chapter introduces synthesis of a stable CsPbBr$_3$ integrated ZIF-8 MOF and explore its dual functional fluorometric sensing behavior towards the detection of p-nitroaniline and rhodamine blue dye. The composite's paper sensor demonstrates the analytes' visual identification ability. The mechanistic pathway of analyte sensing is covered in this chapter, and it is discovered that both analytes respond differently when used with a CsPbBr$_3$@ZIF-8 sensor.
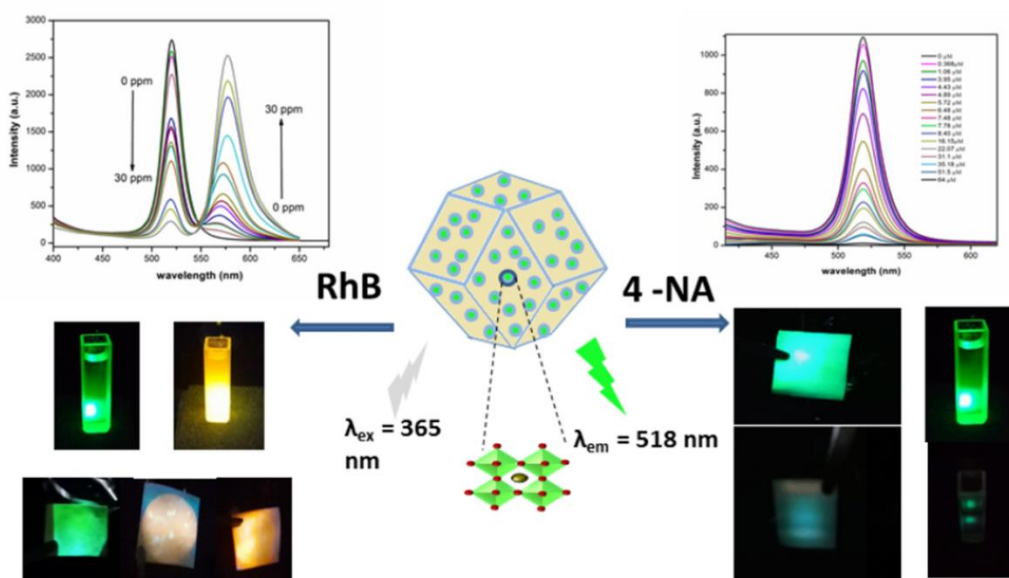
3.1. Introduction

Environmental contamination from different organic pollutants has increased rapidly as a result of industrialization and population growth, drawing attention from all over the world. Excessive use of dye molecules and nitroaromatic compounds (NACs) has been a source of worry due to their negative influence on human health, the environment, and security applications. Nitroanilines are widely utilized as chemical intermediates in many industries, including those that produce insecticides, dyes, plastics, pharmaceutical medicines, agrochemicals, explosives, industrial polymers, etc. [1,2]. However, due to its extreme toxicity, working with nitroanilines, in particular p-nitroaniline (p-NA), might be difficult. These chemicals, which can be found in the wastewaters released by factories, are harmful to both marine life and humans. P-NA has toxicity stronger than aniline and are slowly biodegradable in nature. Through inhalation, ingestion, and skin contact, nitroaniline and its derivatives infiltrate the human ecosystem and cause potentially fatal conditions as blood poisoning, liver damage, dermatitis, and cancer [3-6]. Therefore, lowering the nitroaniline emissions into the environment is strongly suggested. Traditional instrumentation techniques, such as high performance liquid chromatography, surface enhanced Raman spectroscopy, cyclic voltammetry, ion mobility spectroscopy, and X-ray dispersion are being used for the precise detection of p-NA [6-8]. However, because of their high cost, operational complexity, and lack of accessibility, their utility for a fast on spot detection become a limitation.

Rhodamine B (RhB) on the other hand is a common synthetic dye that has found widespread uses in cosmetics, textiles, plastics, and food coloring. The wastewater from textile plants is the most damaging industrial effluent, with as much as 200,000 tons of dyes escaping annually. Aside from this, synthetic dyes can be readily added to food products as a coloring agent to enhance their appearance and compensate for color loss that occurs during food preparation, posing a serious threat to the health of consumers. Therefore, it is urgent to devise a highly sensitive method for selective detection of these organic pollutants [9,10].

In comparison to the conventional analytical method of detection, the fluorometric technique stands out as a simple, inexpensive, fast, highly selective, and sensitive approach for the successful detection of analyte. Smart fluorescent materials that can alter their physical parameters when exposed to an external stimulus have caught the attention of

researchers due to their potential applications in a variety of disciplines such as sensing, anti-counterfeiting, bio-imaging, etc. [11,12]. Most of the luminescent sensing applications are based on organic fluorophores and dyes, polymer nanocomposite, metal oxide nanoparticles, metal chalcogenide quantum dots, etc. [13-15]. However, these materials possess limitations including weak PL intensity, low photoluminescence quantum yield (PLQY), low color purity, photo bleaching, pH dependency, and wide emission line limiting sensitivity of detection. Metal halide perovskite nanomaterials as an alternative, are extremely useful due to their remarkable optical properties and display a number of advantages over its other contemporaries. In light of the advantageous optical properties, $CsPbX_3$ PeQDs have lately been used as chemical and biological sensor materials [16-18]. Due to the instability issue, majority of the analytical applications of $CsPbX_3$ PeQDs are restricted to non-polar medium, thereby making it challenging for practical detection applications. There is only few research work that have been carried out using metal halide perovskite as luminescent sensor materials. Initially, Sheng and their group exploited $CsPbX_3$ PeQDs for the trace detection of Cu^{2+} and Yb^{3+} ion in nonpolar medium like cyclohexane [17]. $CsPbBr_3$ PeQDs were used for the colorimetric detection of HCl vapor by Xiao et al. using anion exchange between Br^- of the PeQD and Cl^- of the HCl [19]. Recently, Xiang et al. and Huangfu et al. utilized the sensitive nature of $CsPbBr_3$ perovskite for the quantification of water content in herbal medicines and total polar material count in edible oils [20,21]. Chen and his groups employed $CsPbBr_3$ quantum dots for the detection of picric acid and other nitroaromatic explosives in nonpolar medium [22].

A subclass of microporous MOF called zeolitic imidazolate framework (ZIF-8), which has excellent chemical and thermal stability as well as good dispersibility, is a suitable platform for the growth of various nanoparticles [23,24].
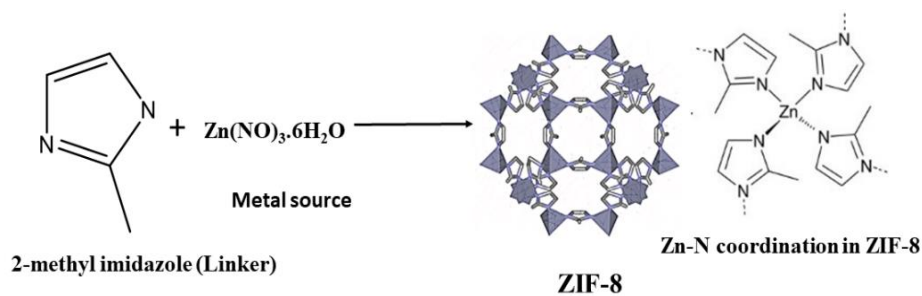

Figure 3.1: ZIF-8 MOF formation and the coordination of Zn metal ion with the linker.

Here, in this chapter CsPbBr$_3$ (CPB) PeQDs are introduced in the ZIF-8 MOF matrix to produce CPB-ZIF-8 heterostructure using an in-situ, one-step technique, and established its excellent stability in aqueous and other polar solvents for the fluorometric detection of organic pollutants RhB dye molecules and NACs. Among various NACs, nitroanilines were found to be the most effective quenchers for CsPbBr$_3$ anchored ZIF-8 MOF. Finally, we have utilized a paper based test strips for on spot detection of p-NA and RhB dye.

3.2. Experimental Part

3.2.1. Materials

All the chemicals used in this work were purchased from commercial vendors and used exactly as received without any further modification. Zinc nitrate hexahydrate (Zn(NO$_3$)$_2$.6H$_2$O), 2-methyl imidazole (HmIM) and dyes were provided from SRL chemicals. Lead bromide (PbBr$_2$), Cesium bromide (CsBr) and all the solvents used were purchased from alfa aesar company.

3.2.2. Methods

3.2.2.1. Synthesis of ZIF-8

A common procedure of ZIF-8 synthesis involves mixing a methanolic solution of HmIM (656.8 mg, 8 mmol) with 2 mmol (595 mg) of Zn(NO$_3$)$_2$.6H$_2$O at a metal to linker ratio of 1:4. After one hour of stirring at room temperature, the mixture turns milky white and the nanocrystals precipitates were separated from the dispersion through centrifugation followed by several washing steps with methanol. After that, the as produced MOF crystals were vacuum dried at 60°C for an entire 24 hours.

3.2.2.2. Synthesis of CsPbBr$_3$@ZIF-8 composite

The MOF matrix is used to grow the perovskite quantum dots using an in-situ, one-step process. Both the ZIF-8 MOF precursors and the CsPbBr$_3$ precursors are combined in this technique. Typically, 1 mmol Zn(NO$_3$)$_2$·6H$_2$O (297 mg) in 6 ml methanol was added into a 6 ml methanolic solution of 2- methylimidazole (328.4 mg, 4 mmol). Separately, 0.5 mmol of CsBr and PbBr$_2$ were dissolved in 5 ml DMF with 0.16 ml OA and 0.045 ml OAm and stirred to form a clear precursor solution. This perovskite precursor solution was then mixed with the MOF precursor and stirred vigorously the mixture for 1.5 hour at room temperature. Then, the solvents were decanted and 10 ml of toluene was added in to the reaction mixture and stirred continuously for 3 h. The products were separated by filtration

and washed thoroughly with methanol. Following washing, the collected materials were vacuum-dried at 80°C for four hours.

3.2.2.3. Sample preparation and sensing measurement

For nitroaniline sensing 5 mg ml^{-1} CPB@ZIF-8 composite was dispersed in methanol and sonicated for 10 min to become homogeneous. Then the PL emission was measured using the 3 ml dispersion of composite. Separately, different concentration of nitroanilines (0 - 64 µM) are prepared in methanol by diluting a stock solution of 1mM. Thereafter, for sensing experiment 100 µl of different concentrations of analyte (0–64 µM) were continuously added into CPB@ZIF-8 standard and incubating at room temperature for 60 sec. Using a 1cm^3 quartz cuvette, the PL emission spectra of the solutions were measured at an excitation wavelength of 365 nm and an slit width of 10 nm.

For the detection of RhB dye, first a 0.1 mM aqueous stock solution was prepared and then diluted to various concentrations. Once the RhB solution was ready, 100 µl of the solution was added to 3 ml of CPB@ZIF-8 dispersion and the mixture was homogenized. The PL spectra were obtained at an excitation wavelength of 365 nm following an incubation period of 2 minutes at room temperature.

3.2.2.4. Preparation of paper sensor: To prepare a paper sensor for the purpose of studying the visual detection of analytes by the CsPbBr$_3$@ZIF-8, square size (1.5 cm×1.5cm) cellulose filter papers were used. Thereafter, the paper strips were dripped into 5 ml of 1.5 mg/ml CPB@ZIF-8 dispersion for 30 min. After room temperature drying process, 4-NA of concentration 0-10µM was dropped into the test strips, forming a simple and low cost visual sensing platform. Similar procedure was followed for RhB dye paper sensor preparation.

3.2.2.5. Quantum yield measurement: The relative PLQY of the composite was measured using fluorescein as the reference standard (Quantum Yield = 0.95 in 0.1 M NaOH). The relation and the procedure used to calculate the PLQY was mentioned in chapter 2 (section 2.2.2.5)

3.2.2.6. Energy level determination of CPB@ZIF-8: For the preparation of working electrode, 5 mg of the synthesized composite was dispersed in 100 µl isopropanol and sonicated for 15 min. Then 30 µl of this dispersion was drop casted on a glassy carbon electrode (GCE, diameter 3 mm) and dried at room temperature. A 0.1 M

tetrabutylammonium hexafluorophosphate (TBAPF$_6$) in acetonitrile solution was acted as supporting electrolyte. The CV measurements were carried out at a scan rate of 50 mV s^{-1}. The energy levels were determined using following relations-

$E_{HOMO} = -$ (E onset, ox + 4.8) eV

$E_{LUMO} = Eg + E_{HOMO}$, where E$_g$ = band gap = 2.42 eV for CsPbBr$_3$/ZIF-8

E onset, ox is the onset oxidation potential.

3.2.2.7. Instrumentation techniques

The structural and morphological characterization of the prepared samples was analyzed using FTIR, XRD, XPS, EDX, FESEM, TEM, and BET method. The optical properties were studied by UV-Vis and photoluminescence spectroscopy. The A Bio-Logic SP-150 potentiostat was used for CV measurement of the composite with a standard three-electrode arrangement. Details of the instruments used to perform the analyses are the same as described in chapter 2 (section 2.2.2.6).

3.3. Results and discussion

The CPB@ZIF-8 hybrid composite was synthesized following an in-situ, one-step process, by growing CPB QDs inside the ZIF-8 MOF cavities throughout the formation process of MOF [25]. Scheme 3.1 illustrates the synthesis strategy of perovskite MOF composite material. Various analytical techniques were used to examine the synthesized materials.
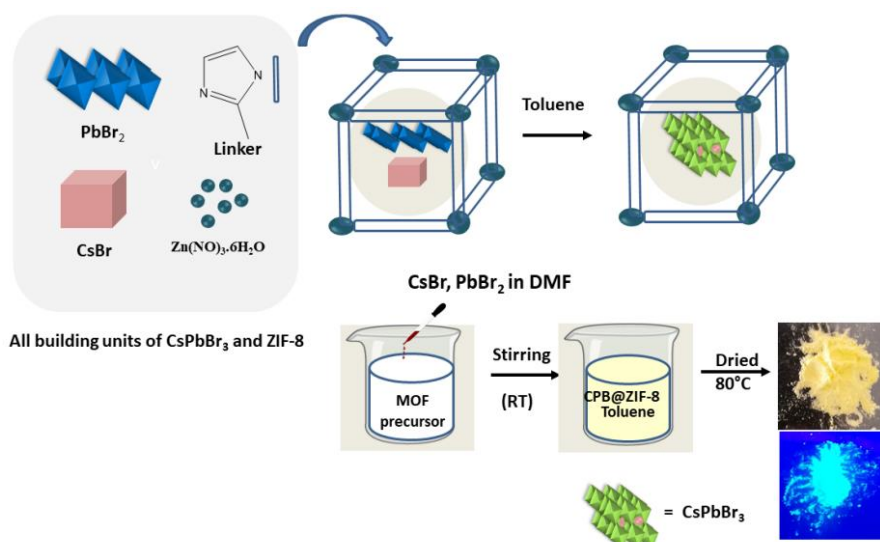
Scheme 3.1. Schematic of one step synthetic path for luminescent CsPbBr$_3$@ZIF-8 composite.

3.3.1. Structural analysis
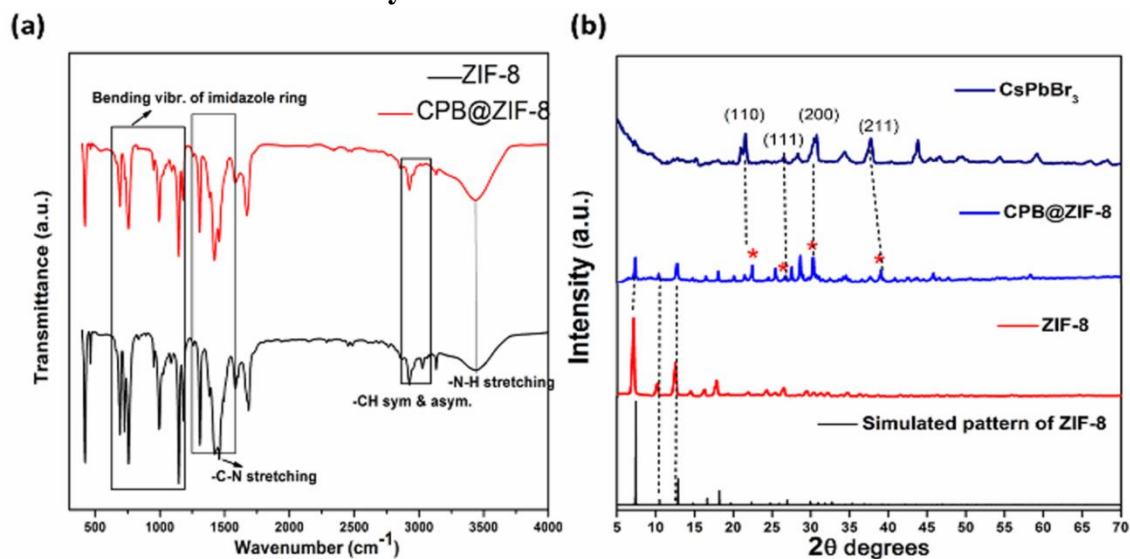
3.3.1.1. FTIR and XRD analysis

Figure 3.2: FTIR spectra ZIF-8 and CsPbBr$_3$@ZIF-8 (a), and P-XRD diffraction pattern of ZIF-8, CsPbBr$_3$, and CsPbBr$_3$@ZIF-8.

FTIR spectra are displayed in Figure 3.2a for ZIF-8 and CPB@ZIF-8. In the FTIR spectrum of ZIF-8, the peaks at around 3190 cm^{-1} and 2933 cm^{-1}, attributed to the C−H stretching vibrations of C−H of the methyl group of ZIF-8. The N-H stretching vibration displayed a peak at 3400 cm^{-1}. All the peaks in the region of 500−1600 cm^{-1} are resulting from the stretching and bending vibration of the imidazolate ring of ZIF-8 and CPB@ZIF-8 [26]. The C−N absorption band of ZIF-8 shows strong peaks in the region 1100–1400 cm^{-1}. The characteristic Zn-N vibration bonding was assigned a peak at 421 cm^{-1}, observed for both ZIF-8 and CPB@ZIF-8, indicating the coordination of Zn^{2+} with the 2-methylimidazole ligand. The FTIR spectrum of CPB@ZIF-8 possessed the characteristic vibrations of ZIF-8, demonstrating the combination of CPB nano crystals (NCs) with the ZIF-8 MOF matrix.

The XRD pattern of the ZIF-8 MOF in Figure 3.2b appears characteristic diffraction peaks at 2θ = 7.60, 10.57, 12.85, 14.8, 16.6, 18.12, that corresponding to the (011), (002), (112), (022), (013), (222), planes of ZIF-8. Very sharp XRD peaks of ZIF-8 matched their standard simulated pattern (CCDC: 864309) [27]. It signifies its phase purity and high crystallinity of the MOF lattice. The prominent peaks of ZIF-8 were appeared in the P-XRD patterns of CPB@ZIF-8 composite. Aside from the ZIF-8 XRD peaks, the diffraction

peak observed at around $21.6°$, $26.6°$, $30.6°$ and $38.6°$ assigned to the (110), (111), (200) and (211) planes of $CsPbBr_3$ PeNCs [28]. A minor shift of the distinctive XRD peaks of $CsPbBr_3$ in the composite was noticed indicating an insignificant disturbance of the CPB lattice with the binding of the MOF matrix.

3.3.1.2. EDX and XPS analysis

(a)

Element	Weight%	Atomic%
C K	40.53	55.06
N K	30.73	35.79
O K	2.58	2.63
Zn K	26.16	6.53
Totals	100	

(b)

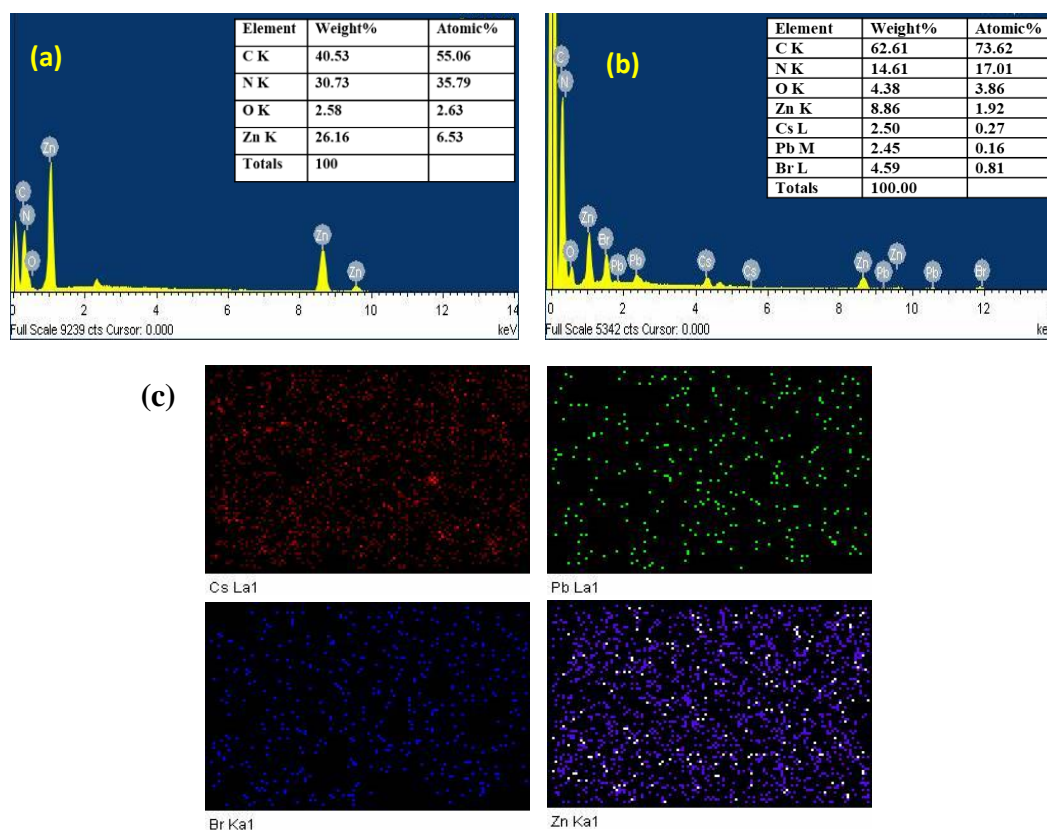| Element	Weight%	Atomic%
C K	62.61	73.62
N K	14.61	17.01
O K	4.38	3.86
Zn K	8.86	1.92
Cs L	2.50	0.27
Pb M	2.45	0.16
Br L	4.59	0.81
Totals	100.00	

Figure 3.3: EDX spectra of ZIF-8 MOF (a), CPB@ZIF-8 (b), EDX elemental mapping of Cs, Pb, Br, Zn elements of CPB@ZIF-8 (c).

Figure 3.3a shows the presence of C, N, Zn in the EDX spectrum of ZIF-8 MOF. The CPB@ZIF-8 composite exhibited the signal of Cs, Pb, and Br along with the component elements (Zn, N, C) of pristine MOF signifying the successful incorporation of $CsPbBr_3$ perovskite in ZIF-8 MOF matrix. Moreover, the elemental mapping of the composite in Figure 3.3c reveals the uniform distribution of $CsPbBr_3$ PeNCs throughout the MOF matrix.

The XPS analysis of CPB@ZIF-8 MOF composite was further conducted to investigate the surface characteristics and elemental state. The characteristic signals of Cs, Pb, and Br

coupled with the C, N, and Zn elements from MOF matrix were detected in the XPS survey spectrum (Figure 3.4a). Cs $3d$ displayed two peaks of Cs $3d_{5/2}$ (725 eV), Cs $3d_{3/2}$ (738.5 eV) and Pb $4f$ showed two peaks of Pb $4f_{7/2}$ (138.8 eV), Pb $4f_{5/2}$ (143.8 eV). Also, the Br 3d fine spectrum was divided into Br $3d_{5/2}$ (67.4 eV) and Br $3d_{3/2}$ (69.2 eV) which correlate to the inner and surface ions of Br. All these peaks are features peaks for $CsPbBr_3$ in the MOF matrix [29]. In addition, the binding energies (BE) of Zn 2p was observed at 1021 eV and 1044 eV (Figure 3.5d) corresponding to the Zn $2P_{3/2}$ and Zn $2P_{1/2}$ states from the ZIF-8. The C$1s$ fine spectrum was fitted into three peaks at 284.5 eV (C-H/ C=C), 285.4 eV (C-N), and 288.2 eV assigning to the N-C=N bond of imidazole ring (Figure 3.4b). Similarly, the N1s spectrum could be deconvoluted into three peaks centered at 398.05 eV, 399 eV, and 399.9 eV. The BE at 398.05 eV attributed to the N-Zn coordinate bond and the peaks at 399.9 eV and 399.9 eV mainly contributed to the N-C (sp^3) and (sp^2) N=C moieties (Figure 3.4c) of the MOF. The results of the XPS study support the production of $CsPbBr_3$ in the ZIF-8 MOF matrix.
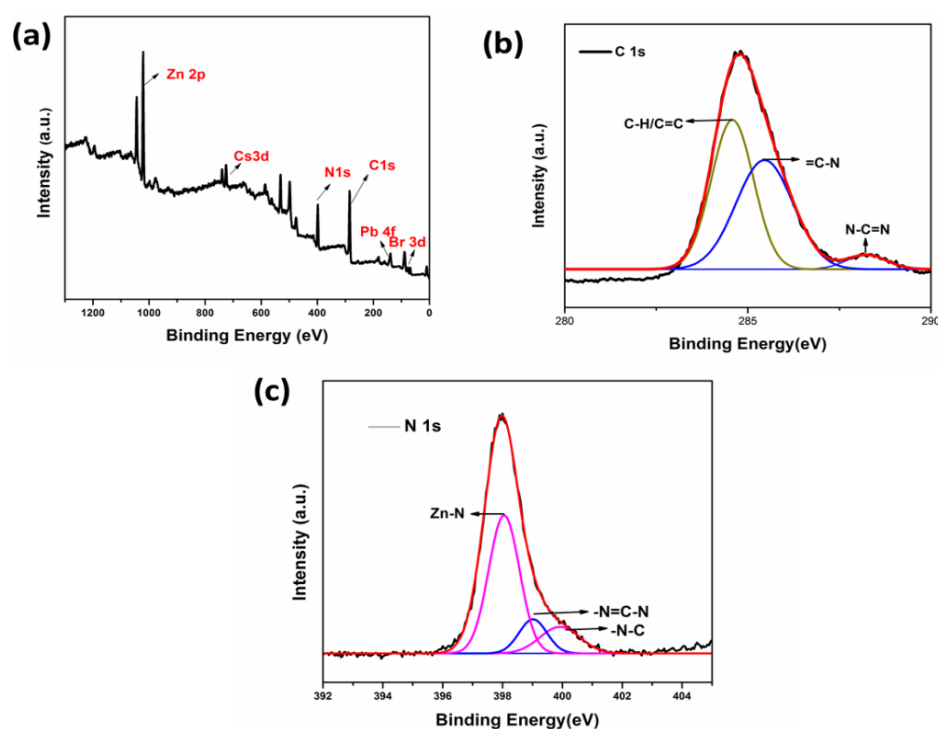

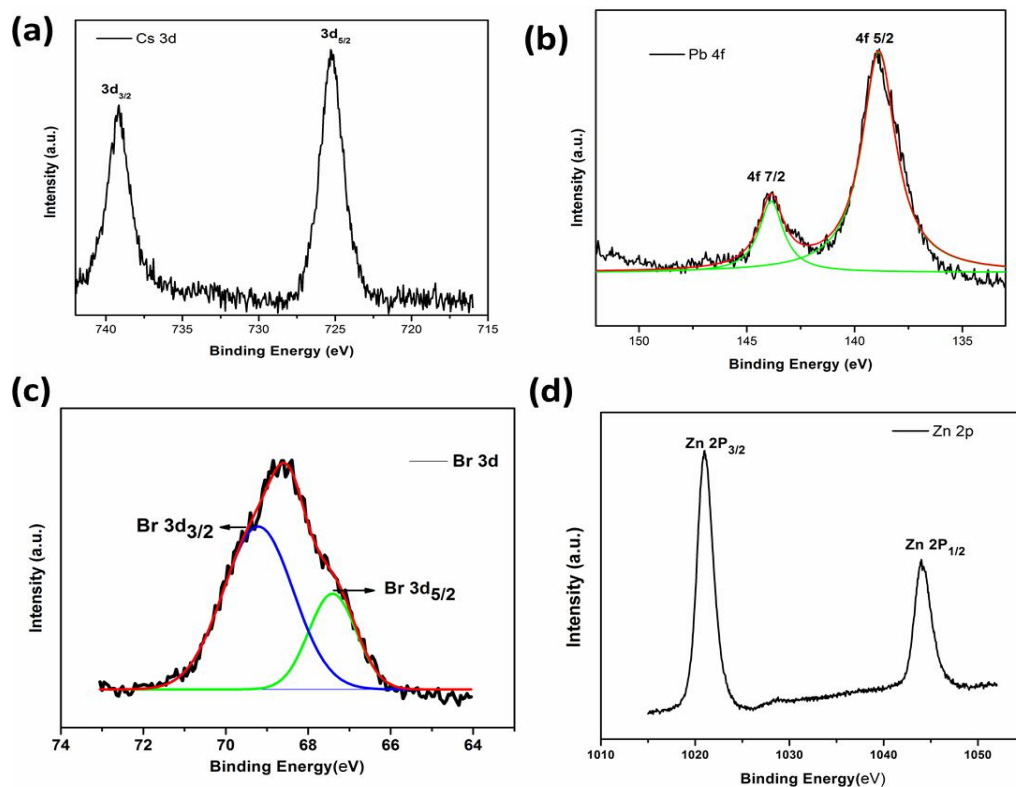**Figure 3.4:** XPS full survey spectrum (a), C$1s$ and N$1s$ high resolution XPS spectra (b, c) of CPB@ZIF-8.

Figure 3.5: XPS spectra of Cs *3d* (a), Pb *4f* (b), Br *3d* (c), and Zn *2p* of CPB@ZIF-8.

3.3.2. Morphological analysis

SEM images were taken to study the surface morphology of CPB@ZIF-8 composite. Figure 3.6c revealed the formation of monodisperse regular smooth rhombic do decahedron crystal morphology for CPB@ZIF-8 composite. The particle size was found in the range of 100 to 220 nm. It has a uniform size distribution with an average size of about 140 nm. The CPB@ZIF-8 retains the surface morphology of pristine ZIF-8, reflecting the stability of ZIF-8 MOF after the incorporation of CPB guest. Figure 3.6a and b display the TEM images of CPB@ZIF-8 composite where CPB PeQDs are well embedded in the MOF matrix. HRTEM images reveals that the distinct lattice fringes have inter planar spacing of 0.26 nm, assigning to the (210) plane of CPB PeQDs.
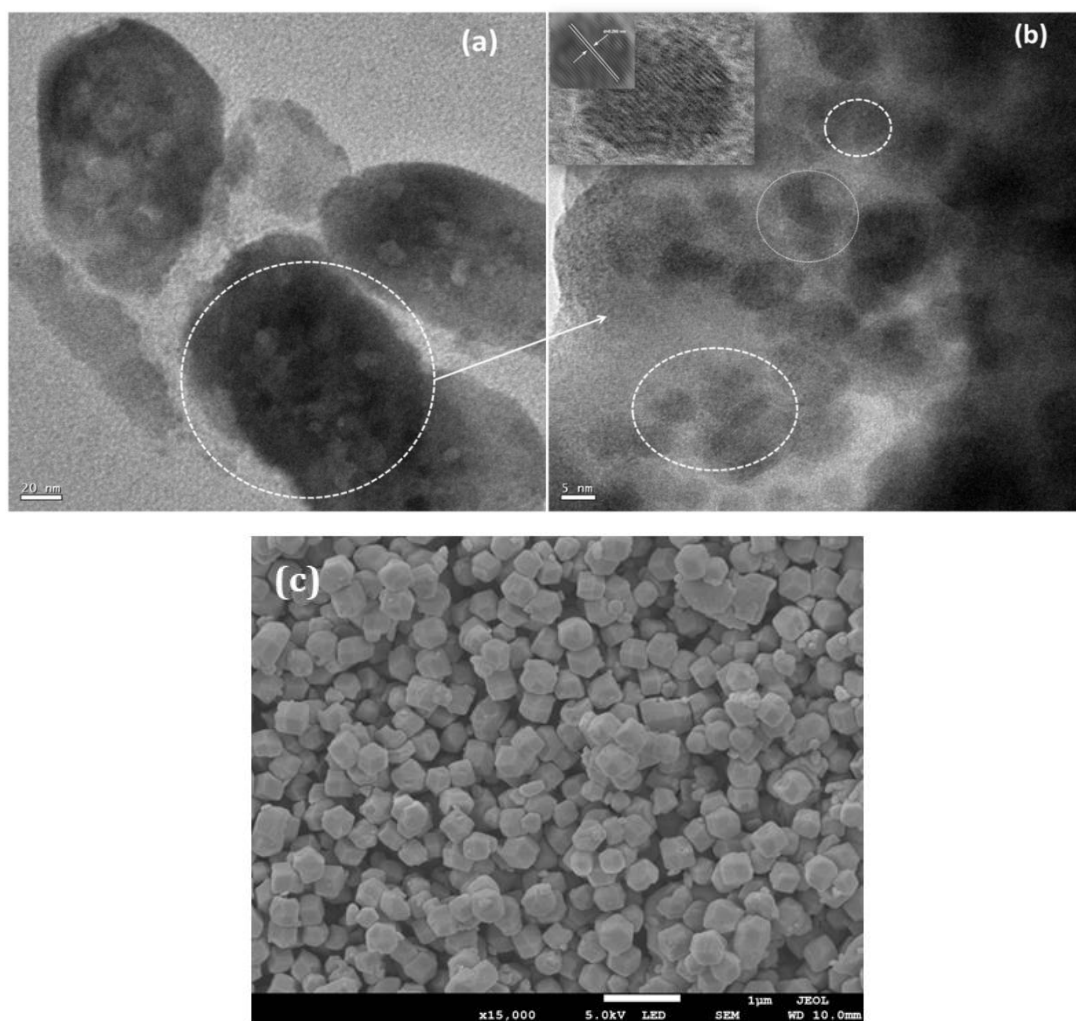
Figure 3.6: TEM and HRTEM images of CPB@ZIF-8 composite (a, b), SEM image of CPB@ZIF-8 (c).

3.3.3. BET analysis

Moreover, the successful introduction of CPB NCs to the ZIF-8 was confirmed by the reduced nitrogen uptake in the N_2 adsorption-desorption isotherm which resulted in the reduction of BET surface area after the incorporation of CPB NCs. BET isotherm and pore size distribution graph was illustrated in Figure 3.7a, and 3.7b. Both the surface area and pore volume of ZIF-8 was reduced after the introduction of CPB PeNCs into the MOF (Table 3.1)
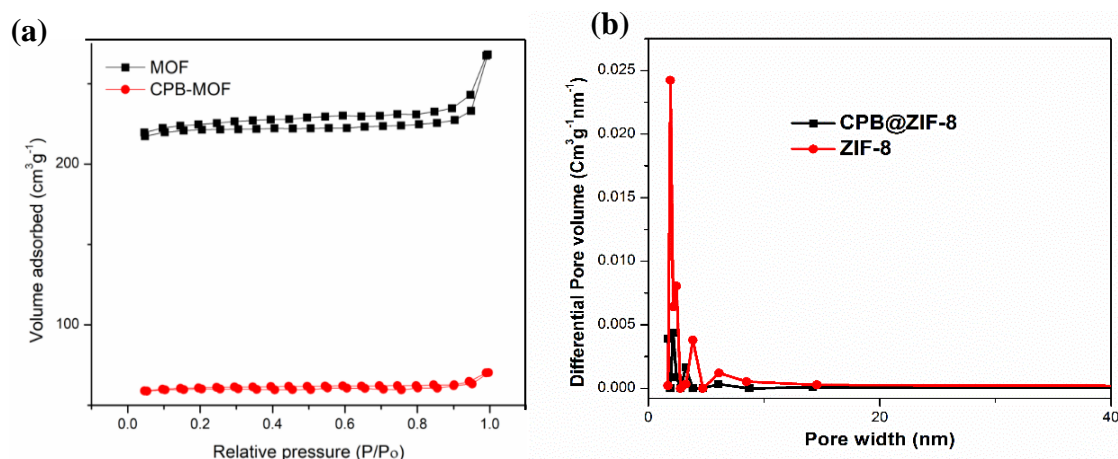
.

Figure 3.7: N_2 absorption-desorption isotherm and pore size distribution graph of pristine MOF and CPB@ZIF (c).

Table 3.1 Summary of Parameters derived from BET isotherm of ZIF-8 MOF and CPB/ZIF-8

Sample	Surface area (m^2g^{-1})	Pore Volume (cm^3g^{-1})	Pore Size (nm)
ZIF-8	627.734	0.070	4.27
CPB@ZIF-8	170.558	0.016	3.09

3.3.4. Optical Properties

Optical properties of CPB@ZIF-8 composite were investigated to understand the absorption and emission behavior of the composite (Figure 3.8). The absorption spectrum of CPB@ZIF-8 powder exhibits a strong characteristic peak of $CsPbBr_3$ perovskite at 515 nm (2.4 eV). When excited at 365 nm wavelength, we have seen the intense green emission peak of CPB@ZIF-8 at 518 nm with a very narrow FWHM value of 20 nm. The relative PLQY of the composite with respect to fluorescein was found to be 51.3% which is higher in comparison to the $CsPbBr_3$ powder without MOF matrix (24.5%). Time resolved photoluminescence measurements of CPB@ZIF-8 composite was performed at an emission wavelength of 518 nm. The carrier lifetime of CPB@ZIF-8 can be calculated using the TRPL decay dynamics where the average lifetime of the composite was found to be 26.03 ns. The bi-exponential function $Y = Y_0 + A_1 \exp(-x/\tau_1) + A_2 \exp(-x/\tau_2)$ was used to fit the decay curves (Figure 3.8b), and Table 3.4 highlights the decay parameters.

The decay process involved two components, a fast process (τ_1 = 1.44 ns) and a slow process (τ_2 = 35.17 ns). Also, CPB@ZIF-8 has higher average lifetime than the pristine CPB (τ_{avg}= 18.20 ns). This indicates the reduction of surface trap states of $CsPbBr_3$ by the protection of ZIF-8 matrix that restricts the nonradiative recombination process, is consistent with the high PLQY of CPB@ZIF-8.
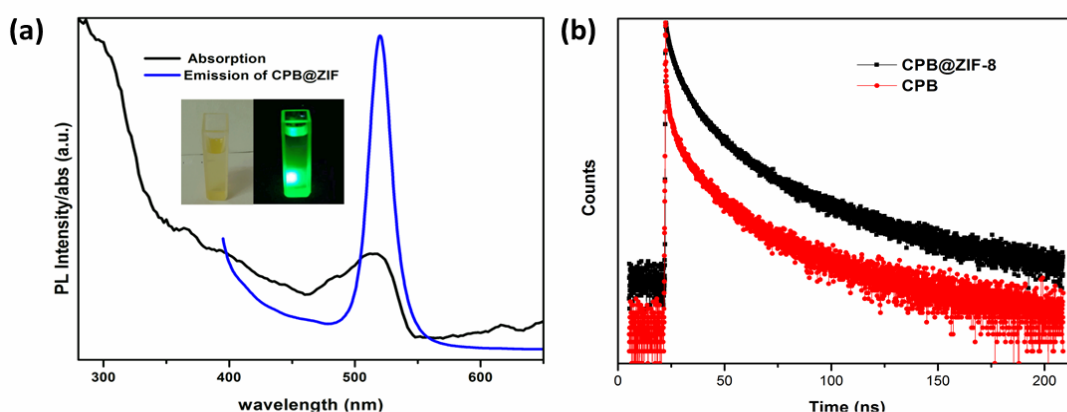

Figure 3.8: Absorption (black) and emission (blue) spectra of CPB@ZIF (a) inset shows the CPB@ZIF-8 dispersion under 365 nm UV irradiation (right) and daylight (left), TRPL decay curve of $CsPbBr_3$ (Red) and CPB@ZIF-8 (black) (b).

3.3.5. Stability investigation of CPB@ZIF-8 composite

CPB@ZIF-8 composite powder was stored in ambient environment for months. The PL spectra evolution of the composite in toluene after two months in humid condition (~60% humidity) shows negligible change in emission intensity whereas the PL intensity of CPB QDs without MOF matrix was quenched (Figure 3.9c and d), indicating long term storage stability of the composite in ambient condition. The CPB@ZIF-8 composite's photo stability experiment was carried out by exposing the sample to 365 nm UV light in an ambient setting while periodically measuring the emission intensity. The composite retains 78.1% of its initial PL intensity after 48 hours of exposure. The composite's solvent stability study was put to the test by soaking the powder in a variety of polar solvents for seven days while analyzing their PL emission spectra. Figure 3.9a shows that the composite retains its emission intensity over a long period of time, indicating solvent resistance capacity.
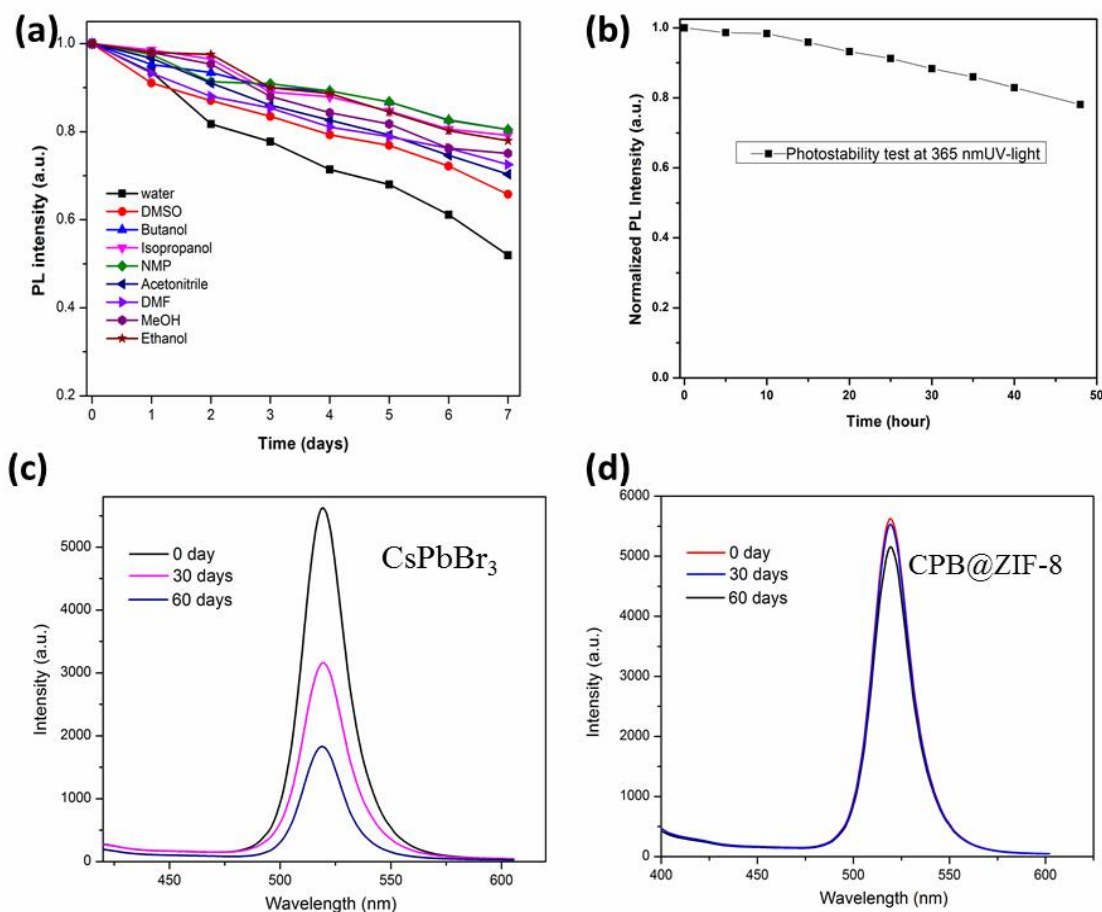
Figure 3.9: Intensity variation of CPB@ZIF-8 as a function of time with various solvents (a), Photostability test of the composite for 50 h (b), Storage study of bare CPB (c) and CPB@ZIF-8 (d).

3.3.6. Luminescence sensing performances of CPB@ZIF-8

The superior optical properties and aqueous stability of the CPB@ZIF-8 composite make it suitable for fluorescence (FL) assays of target analytes. This study investigates the potential applicability of CPB@ZIF-8 as a fluorescence probe for the detection of p-NA and RhB dye.

3.3.6.1. Detection of 4-Nitroaniline

As was previously mentioned, the excellent luminescent properties of the CPB@ZIF-8 sensor prompted us to explore its possible applications in the detection of aromatic pollutants. The luminescence response of CPB@ZIF-8 sensor to different nitro aromatics was evaluated by gradually adding the analyte in methanol to the CPB@ZIF-8 suspension. For our initial round of aromatic analytes, we selected some of the common substances

like benzene, toluene, phenol, nitrobenzene and aniline. Among these, only 500 µl of .085 mM nitrobenzene quenches 24 % of PL signal of CPB@ZIF-8 (Figure 3.10). This outcome motivates us to further investigate the detection potential of CPB@ZIF-8 for other NACs in more detail.
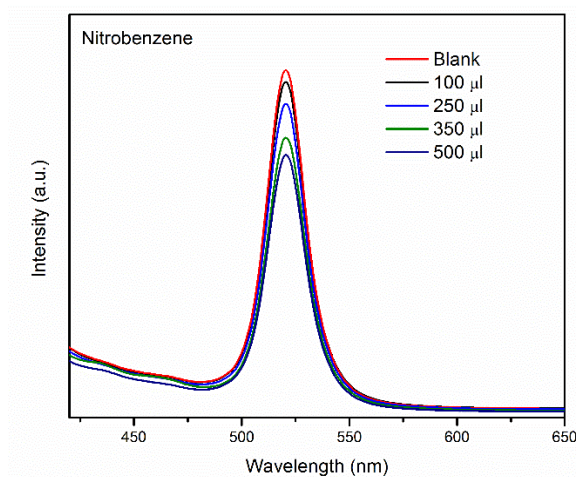

Figure 3.10: PL emission response of CPB/ZIF-8 with various concentration of nitrobenzene.

Then we performed the FL titration test with p-nitroaniline (p-NA) to examine the applicability of CPB@ZIF-8 for p-NA detection. The luminescence intensity at 520 nm was decreased continuously with the increase in concentration of p-NA ranging from 0 µM to 64 µM (Figure 3.11a) and the peak was almost quenched completely with quenching efficiency (QE) equal to 98% when the concentration of p-NA reached up to 64 µM. Then, we studied the quenching performance of the sensor with p-NA by using the Stern-volmer relation, $F_o/F = 1+K_{SV}[C_{4-NA}]$. Here, F_o and F is the intensity of the blank sample and after the addition of p-NA respectively, $[C_{4-NA}]$ represents p-NA concentration. As illustrated in Figure 3.11b, the intensity versus concentration curve followed a good linear relationship from 0.368 to 51.5 µM having a correlation coefficient R^2 of 0.99058. The Stern-volmer constant (K_{SV}) for p-NA sensing was calculated to be 5.942×10^5 M^{-1}. An extremely low theoretical detection limit (LOD) of 60.58 nM (8.367 ppb) was calculated using 3σ/S, (where S is slope of the linearly fitted graph and σ signifies standard deviation of the blank sample).
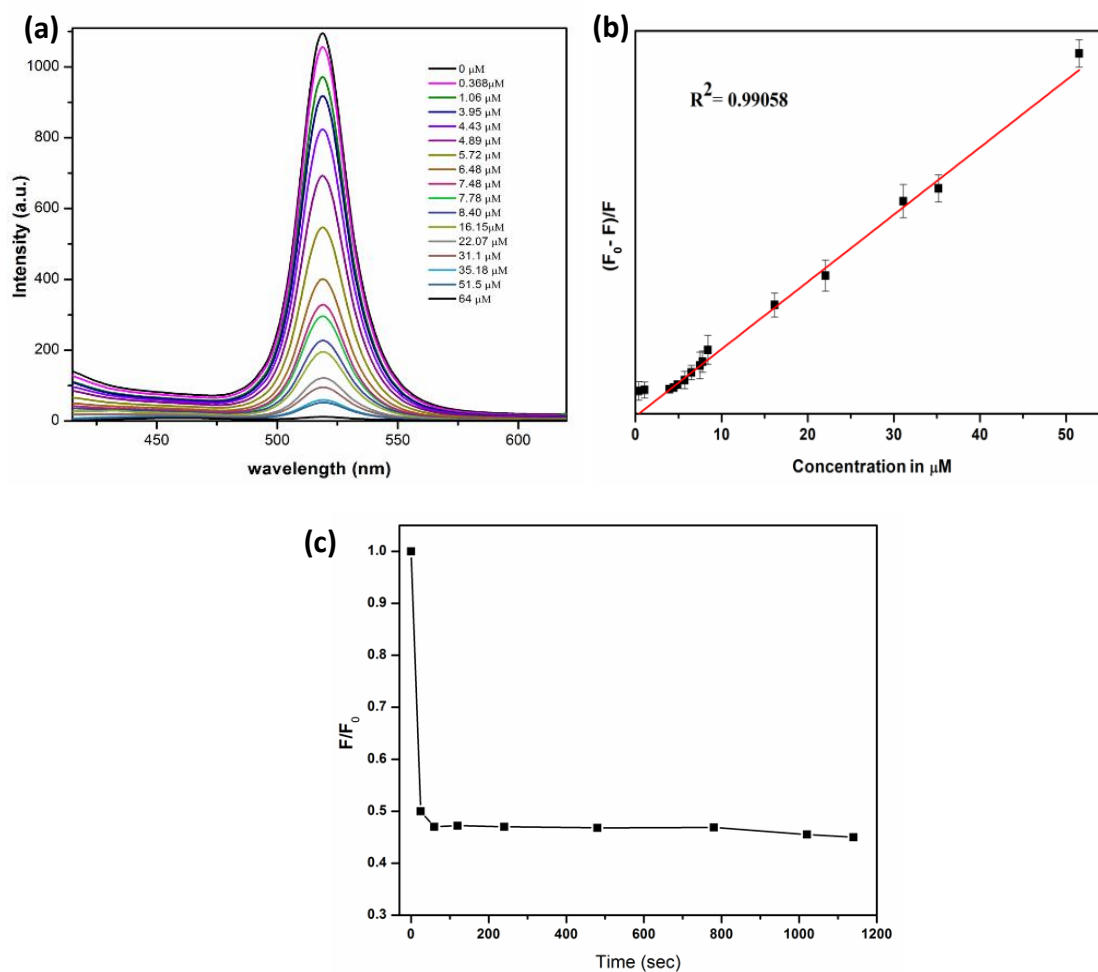
Figure 3.11: Emission spectra of CPB@ZIF-8 with various concentrations of p-NA (a), Calibration graph versus concentration of p- NA (b), Change in PL intensity vs. time graph with p-NA addition for 1200 sec incubation period (c).

The sensing performance of this system for p-NA was compared to previous findings on NACs sensing (Table 3.2) and found a comparable result and even better than some of the previous reports on p-NA recognition. Also, the quenching with p-NA proceeded so rapidly within 25 sec and it becomes stable after 60 sec with no significant change in intensity was observed up to 1200 sec (Figure 3.11c), indicating the system's fast response towards the analyte molecule.

Table 3.2. Comparison of performance of CPB@ZIF-8 FL sensor with previously reported literatures for 4-nitroaniline detection.

Fluorescent System	LOD (nM)	K_{SV}	Linear range (M)	Ref
Cd– PDA MOF	25 nM	$4.0\,7\times10^4$ M^{-1}	0−10 μM	[1]
Porous organic polymer (TPDC-DB)	455 ppb	1.7×10^4 M^{-1}	N/A	[2]
Cd MOF	0.52 ppm	9.8×10^4 M^{-1}	0 − 0.0001 M	[3]
FJI-H26 MOF	0.025 mM	4.1×10^4 M^{-1}	0.005 − 0.025 mM	[4]
1,2,3-triazolyl based conjugated microporous polymer	4.2 μM	7.08×10^4 M^{-1}	0.5–4 μM	[5]
N-doped carbon dots (Blue) Green	111.6 nM 68.9 nM	$1.4 \pm 0.2 \times 10^4$ M^{-1} $2.9 \pm 0.1 \times 10^4$ M^{-1}	0 − 40 μM 0− 50 μM	[30]
Triphenylamine functionalized sensor	724 nM (0.10 ppm)	2.28×104 M^{-1}	0 – 40 μM	[31]
W-N-CDs and E-N-CDs	1 and 0.1 μM	8.82×10^3 M^{-1} 1.25×10^4 M^{-1}	(0–1) 10^{-4} M (0–0.8) 10^{-4} M	[32]
CsPbBr$_3$@ZIF-8	60.58 nM (8.36 ppb)	5.942×10^5 M^{-1}	0.368 – 51.5 μM	This work

(a) Selectivity test

The quenching of CPB@ZIF-8 with various competitive NACs and organic amine derivatives were explored to evaluate the selectivity of the sensor towards p-NA detection. The CPB@ZIF-8 dispersion was added to different nitroaromatic solutions in methanol including m-nitroaniline (m-NA), o-nitroaniline (o-NA), 2,4-dinitroaniline (2,4-DNA),

phenylene diamine (P-Phe), triethylamine (TEA), p-nitrophenol (p-NP), nitrobenzene (NB), 2,4-dinitrophenol (2,4-DNP) and picric acid (PA), having concentrations similar to that with p-NA. When compared to other NACs, 4-NA exhibited the highest quenching efficiency, indicating the obvious selectivity of CPB@ZIF-8 towards 4-NA (Figure 3.12a). For the practical applicability of this sensing probe, interference effect of few common inorganic metal ions was examined. As discussed in Figure 3.12b, the presence of metal ions had less impact on the p-NA's ability to quench the CPB/ZIF-8 PL signal. To understand the extent of quenching of CPB@ZIF-8 by other NACs (e.g., o-NA, m-NA, PA, 2,4-DNA), stern-volmer relation was applied to them (Figure 3.13 – 3.16). The aforesaid findings indicate that all NACs can diminish FL intensity, however the quenching percentage of each NACs varies significantly. Table 3.3 and Figure 3.12c shows the comparison of sensing capacity of different NACs. The K_{SV} value for 4-NA was found to be the highest, signifies the more sensitive nature of the probe sensor towards 4-NA. Also, we observed a different quenching response among the nitroaniline isomers. The value of quenching constant (K_{SV}) order was found to be 4-NA > 2-NA > 3-NA, indicating the potential of this sensor to differentiate between these three isomers via fluorometric quenching technique.
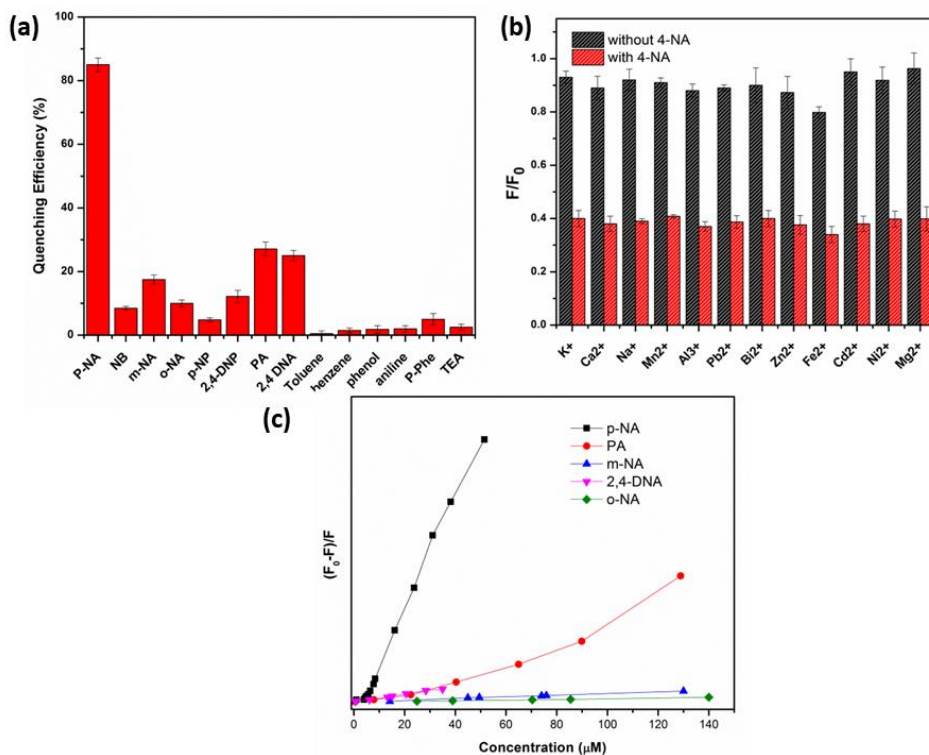

Figure 3.12: Quenching efficiency of various aromatic analytes (a), PL quenching of the CPB@ZIF-8 probe when p-NA was mixed with another metal ion (b), and Variation of PL intensity with various competitive NACs (c).
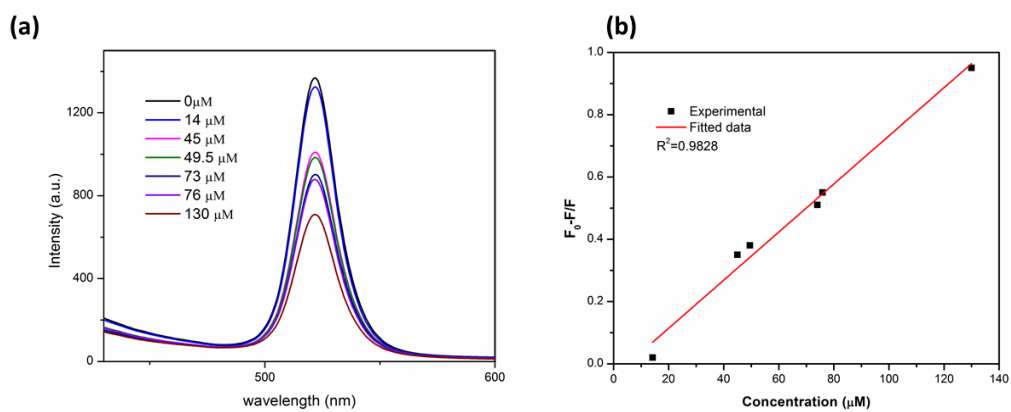
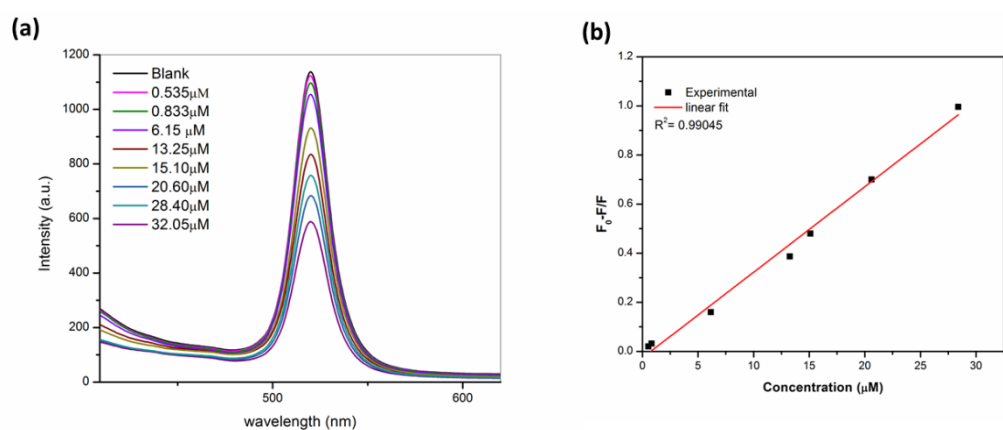**Figure 3.13:** PL response of CPB@ZIF-8 with o-NA (a), Stern-Volmer plot (b).

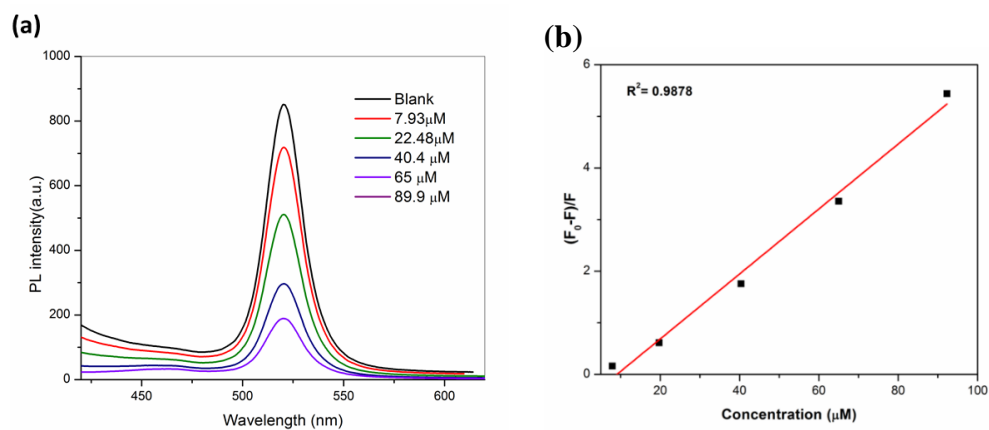**Figure 3.14:** PL response of CPB@ZIF-8 with 2,4 DNA (a), Stern-Volmer plot (b).

Figure 3.15: PL response of CPB@ZIF-8 with PA (a), Stern-Volmer plot (b).
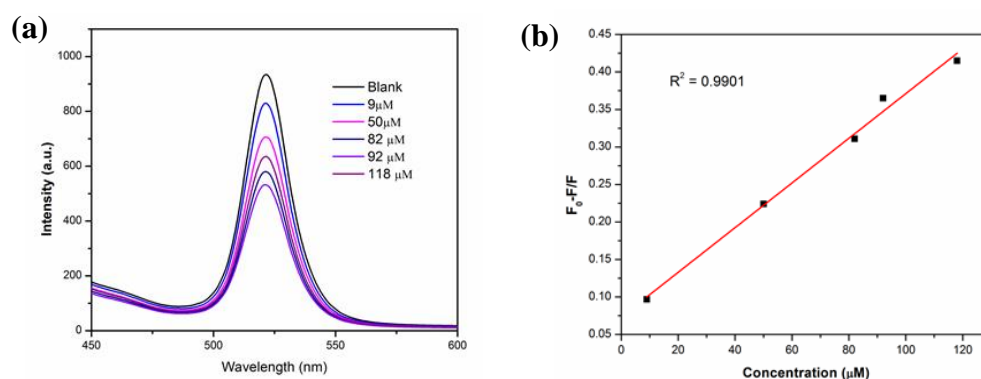
Figure 3.16: PL response of CPB@ZIF-8 with m- NA (a), Stern-Volmer plot (b).

Table 3.3. Comparison of quenching constant (Ksv), LOD and, correlation values of different NACs analytes.

Analytes	K_{sv}	LOD	Correlation coefficient (R^2)
4-nitroaniline	$5.942{\times}10^5$	60.58 nM	0.99058
2-nitroaniline	$7.73{\times}10^3$	0.176 µM	0.98280
3-nitroaniline	$3.18{\times}10^3$	0.186 µM	0.9901
2,4-dinitroaniline	$3.48{\times}10^4$	0.120 µM	0.99045
Picric acid	$6.52{\times}10^4$	0.137 µM	0.9878

(b) Detection of p-NA in paper substrate

The practical applicability of the sensing probe was further examined by constructing a paper based FL sensor. For the on spot detection of p-NA, it was dropped in the prepared paper sensor with increasing concentration between 0-10 µM. With the increase in the concentration of p-NA, green luminescence of the paper strips diminished similar to the liquid phase method under a UV lamp of 365 nm wavelength. Figure 3.17 shows the optical photograph of the test papers with 4-NA contamination. These findings indicate the sensitivity of cheap paper sensor of CPB@ZIF-8 to various concentrations of p-NA.
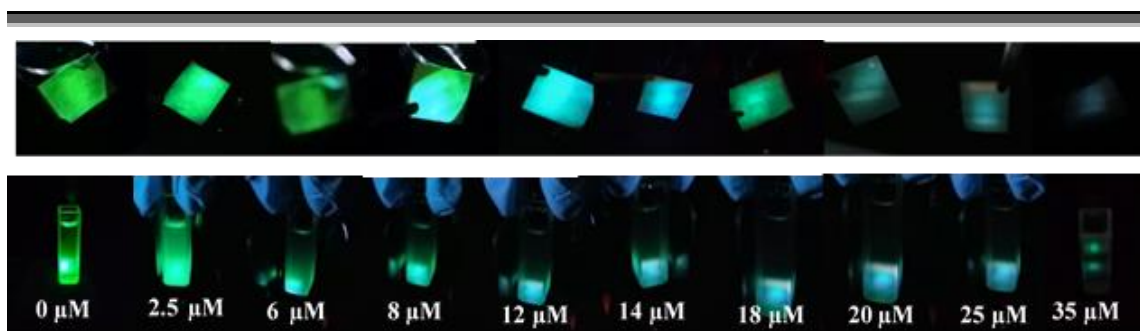
Figure 3.17: Photograph showing the loss of green emission of paper strips with 4-NA addition.

(c) Plausible mechanism of p-nitroaniline sensing

To explore the quenching of the fluorescence signal by 4-NA, 1st we have studied the UV-Vis spectra of 4-NA. As shown in Figure 3.19a, there is no considerable overlap between the UV-Vis absorption spectrum of 4-NA and emission spectrum of CPB@ZIF-8 which eliminates the possibility of energy transfer between the fluorophore and the analyte. Also, the absorption and emission peak of the composite did not show any shift after the addition of 4-NA. The solid UV-Vis spectra of the composite with p-NA exhibited the appearance of 4-NA absorption peak along with the perovskite peak (Figure 3.19b). It reveals that there was no change in the crystal structure of the sensor with the introduction of p-NA, removing the static quenching mechanism.

The electron withdrawing nitro group in p-NA, is stabilized by the delocalization of pi bond energy facilitate through the donation of lone pair electron of $-NH_2$ group. It might generate some strong interactions with the CPB@ZIF-8 MOF composite [3]. Further, FTIR was used to investigate the interaction between p-NA and CPB@ZIF-8 composite. The FTIR spectra of the composite soaked in p-NA solution revealed the presence of N-H bending vibration of p-NA at 1630 cm^{-1}. Both the UV-vis (Figure 3.19b) and FTIR spectra (Figure 3.19d) confirmed that the p-NA was absorbed in the porous channels of MOF matrix. Moreover, a small shift of N-H bending mode was noticed from free p-NA indicating the existence of H-bonding interaction between p-NA and CPB@ZIF-8. Thus, the p-NA molecule binds to the MOF matrix through H-bonding and easily diffuses to the perovskite NCs to quench the perovskite signal. For further verification of the sensing kinetics, TRPL decay measurements were performed. The curves were fitted using a bi-exponential fitting equation (Figure 3.19c). The average lifetime of the sensor was reduced from 26.03 ns to 24.79 ns and 24.13 ns in presence of 3µM and 5.50 µM of p-NA

respectively (Table 3.4). Therefore, a dynamic quenching process was involved where the target analyte reacted with the excited state of CPB@ZIF-8. Moreover, after p-NA treatment the non-radiative component (A_2) of the sensing probe increased from 55.37% to 58.88%, suggesting the increase of defect density of CPB@ZIF-8 which produces some non-radiative recombination pathways and shortened the carrier life time [17, 33, 34].

Most of the previous literatures consider PET (photo-induced electron transfer) from the electron rich donor to the electron deficient nitro compounds as a major quenching mechanism for nitroaromatics detection by luminescent sensing probe. A lower LUMO energy level of acceptor molecule than the LUMO level of donor probe is necessary to occur electron transfer process. But, in this case the LUMO of p-NA (E_{LUMO} = -1.95 eV) [5], which is higher than the E_{LUMO} of $CsPbBr_3$ (-3.41 eV), signifying that the PET is not a feasible process. We can assume that more trap states are introduced into the CPB@ZIF-8 by 4-NA molecule, which leads to the quenching of the PL signal. The HOMO and LUMO levels of $CsPbBr_3$@ZIF-8 composite were determined using Cyclic voltammetry (CV) analysis (details mentioned in the method section).
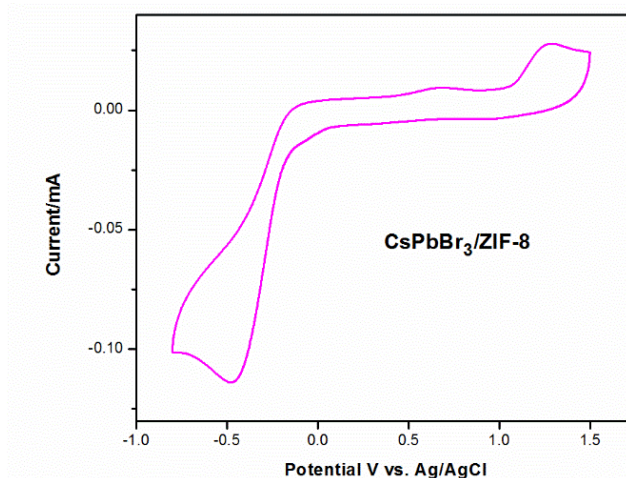

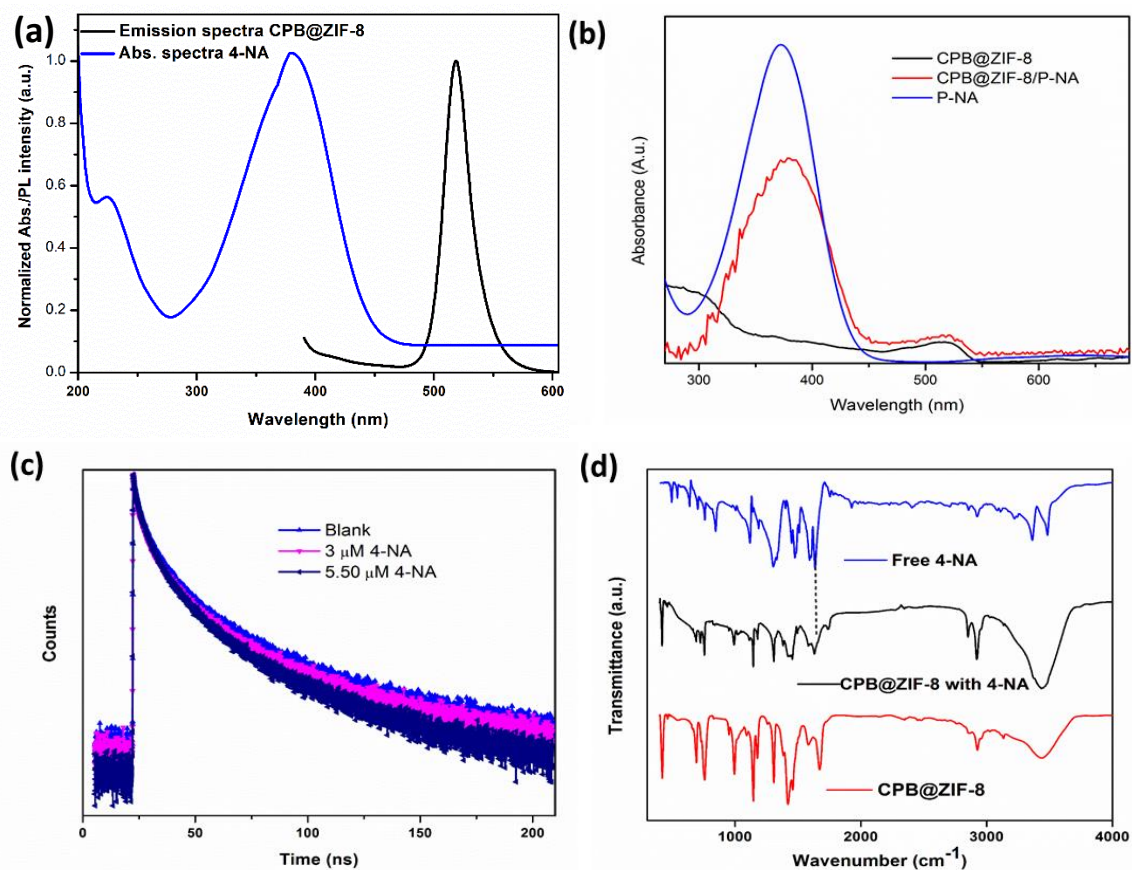**Figure 3.18:** CV profile of CPB@ZIF-8.

Figure 3.19: Absorption spectra of 4-NA (blue), and PL spectra (black) of CsPbBr$_3$@ZIF-8 (a), UV-vis spectra of CPB@ZIF-8 (black), CPB@ZIF-8/4-NA (Red), 4-NA (blue) (b), TRPL decay dynamics of CPB@ZIF-8 with 4-NA addition (c), FTIR spectra of 4-NA (blue), CPB@ZIF-8 (Red) and CPB@ZIF-8 with 4-NA (black) (d).

3.3.6.2. Detection of Rhodamine blue dye

Figure 3.20a shows, the emission spectrum of CPB@ZIF-8 considerably overlaps with the absorption spectrum of RhB in water, fulfilling the requirement for FRET (Fluorescence resonance energy transfer). Therefore, we examine the potential application of detection ability of CPB@ZIF-8 composite by using RhB as target analyte. With the addition of various RhB dye concentrations (100 μM standard dye solution in water) to the aqueous dispersion of perovskite, the emission peak of CPB@ZIF-8 at 518 nm under an excitation wavelength of 365 nm progressively decreased and a new peak arise at 565 nm due to RhB dye (Figure 3.20b). Accordingly, the emission peak at 565 nm enhances, demonstrating that the energy transmitted from CPB QDs through FRET mechanism is absorbed by the fluorescence unit of RhB. Therefore, we can utilize this fluorimetric sensor as ratiometric probe for the detection of RhB dye. Figure 3.20b illustrates the photoluminescence

response of CPB@ZIF-8 solution with an increasing concentration of RhB analyte ranging from 0 – 30 PPM. The fluorescence intensity ratio $I_{dye}/I_{CPB@ZIF-8}$ was used to calibrate the RhB dye concentration. When the intensity ratios were plotted against dye concentrations in the 0 – 30 ppm range (Figure 3.20c), a good linear relationship was found with R^2 value of 0.9907 well fitted to the relation- $I_{565}/I_{518} = 0.1159$ [RhB] $+ 0.035$, where I_{565}/I_{518} is the intensity ratio between RhB dye and CPB@ZIF-8. Noticeably, the LOD has been determined to be 0.088 ppm. The results are comparable with some previously reported studies for detecting various dyes [35-38].
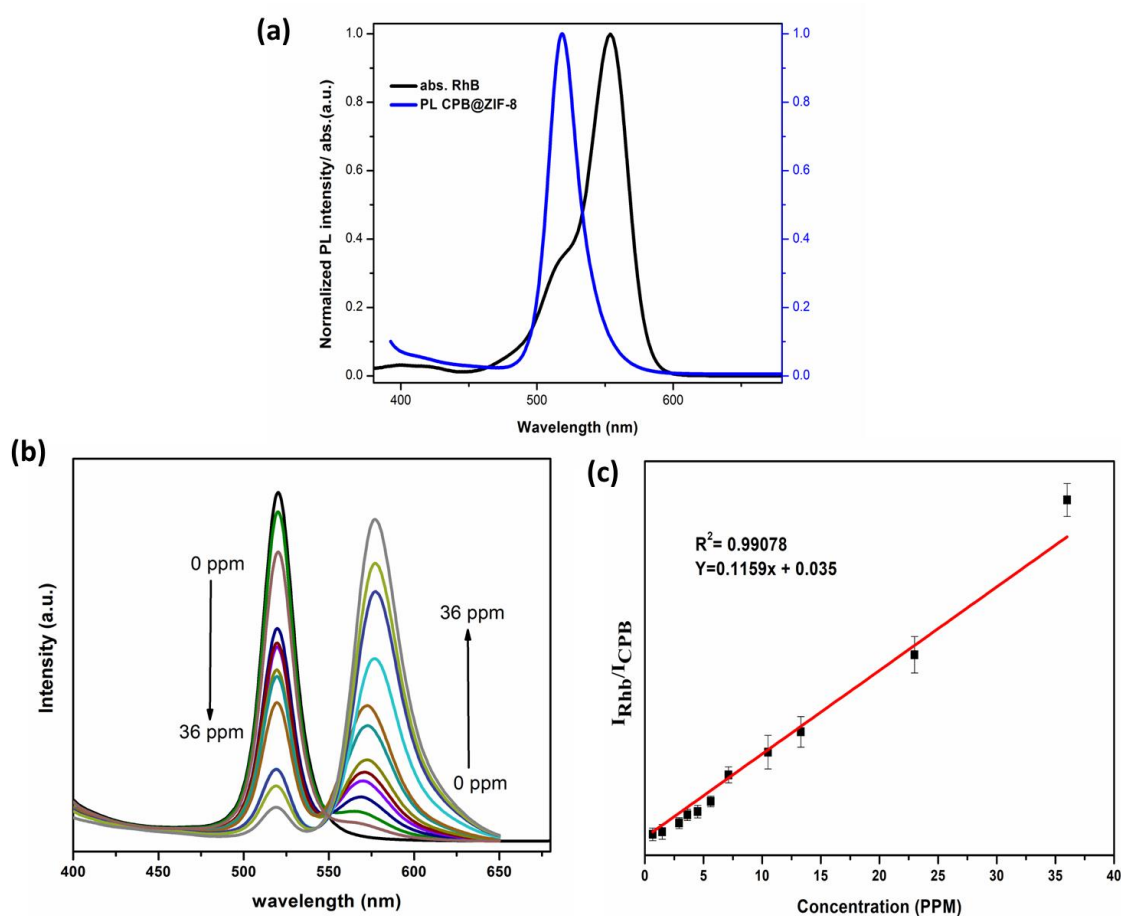
Figure 3.20: Overlapping between the absorption spectrum of RhB (blue) and emission spectrum (black) of CPB@ZIF-8 (a), PL response of CPB@ZIF-8 with increasing concentration of RhB (b), Calibration plot between the ratios $I_{dye}/I_{CPB@ZIF-8}$ vs. concentration of RhB (c).

The sensitivity of the sensing probe was established by the speed with which the quenching took place at 518 nm with RhB addition. The PL signal at 518 nm started to reduce instantly after the RhB addition, and it lasts for the next 2 min. Accordingly, the intensity

at 565 nm starts and it continuously increases for 2 min. After that, there was no discernible change in intensity. Figure 3.21a depicts the graph of PL intensity at 518 nm and 565 nm over a 40 min incubation period in the presence of a specific amount of RhB dye. This outcome validates the system's ability to identify RhB dye irrespective of reaction time.

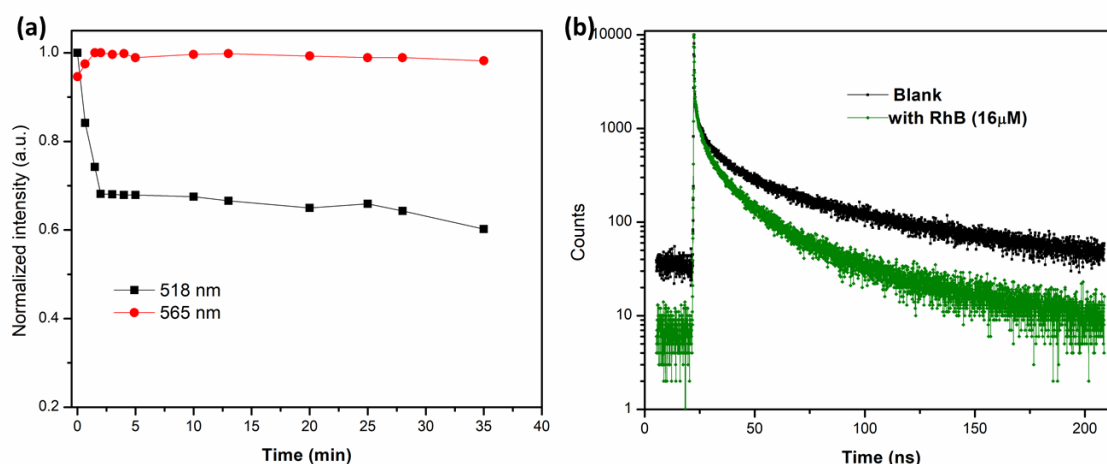**Figure 3.21:** Normalized PL intensity of CPB@ZIF-8 vs. time response plot at 518 nm and 565 nm wavelength (a); TRPL measurement in the presence of RhB (b).

(a) Plausible sensing Mechanism

Numerous processes, such as the Forster resonant energy transfer (FRET), inner filter effect (IFE), electron transfer process, ion exchange process (static quenching), and others, can cause the photoluminescence quenching of a sensing probe. In our instance, the PL spectrum of the CPB@ZIF-8 composite overlaps significantly with the absorption spectrum of the aqueous solution of RhB analyte, satisfying the necessary precondition for FRET based quenching process to occur. In order to better understand the FRET process, lifetime measurement of the CPB@ZIF-8 was examined with RhB dye (Figure 3.21b). RhB's existence caused the composite's lifetime to decrease to 20.9 ns (Table 3.4), providing clear proof existence of energy transfer between donor CPB perovskite and acceptor RhB dye molecules. Using the following equation (1), the FRET efficiency (η) was calculated to be 48.06 % with 5 ppm RhB aqueous solution. τ_{DA} and τ_D represent the lifetime of CPB@ZIF-8 in the presence and absence of RhB respectively.

$$\eta = 1 - (\int PL_{DA}(E)\, dE / \int PL_D(E)\, dE) = 1 - (\tau_{DA}/\tau_D) \qquad (3.1)$$

Furthermore, the forster radius (R_0) which signify the separation radius between the donor and acceptor molecule when 50% of the energy transferred can be calculated using the following equations [37,39]-

$$R_0 = 0.211 \times [k^2 n^{-4} \varphi_d J(\lambda)]^{1/6} \qquad (3.2)$$

$$J(\lambda) = \int_0^\infty F(\lambda) \varepsilon_A(\lambda) \lambda^4 \, d\lambda \qquad (3.3)$$

Here, k^2 represents the orientation factor (2/3) and n denotes the refractive index, 1.54 for ZIF-8 [40]. φ_d is the quantum yield of the donor (51.3 % for CPB@ZIF-8) and $J(\lambda)$ symbolizes the overlapping integral between the donor and acceptor molecule. $F(\lambda)$ in equation (3) describes normalized fluorescence intensity of donor species and ε_A is the molar extinction coefficient of the acceptor. For this sensing system, the R_0 was determined to be 6.37 nm. Moreover, FRET requires both spectral overlap and a near distance ($\leq$ 10 nm) between the two donor acceptor moieties (r), which is another crucial requirement. The porous structure of ZIF-8 MOF which is evident from the BET analysis provides close proximity between the $CsPbBr_3$ and the RhB molecules for energy transfer. FRET efficiency (η) is correlated to the distance r according to the relation, $\eta = R_0^6/(R_0^6 + r^6)$. At the maximum energy transfer efficiency (88.76%) with RhB, the distance r between $CsPbBr_3$ and RhB in ZIF-8 was calculated to be 4.57 nm, which is in the range from 3.18 nm ($0.5R_0$) to 9.5 nm ($1.5R_0$) [40]. All the above discussed results indicate a highly efficient FRET pathway from CPB to RhB can occur in ZIF-8 MOF matrix.

Table 3.4. Summary of TRPL decay parameters

Sample	τ_1 (ns)	τ_2 (ns)	A_1(%)	A_2(%)	τ_{avg} (ns)
CPB@ZIF-8	3.81	28.44	44.63	55.37	26.03
CPB	1.24	18.66	31.46	68.54	18.20
CPB@ZIF-8+4-NA (3µM)	3.77	28.30	42.99	57.01	24.79
CPB@ZIF-8+4-NA (5.5µM)	3.76	26.18	41.12	58.88	24.13
RhB	4.60	25.20	45.16	31.88	20.9

(b) Visual analysis of RhB

With the gradual increase of RhB concentration to the CPB@ZIF-8 sensing probe, we observed a distinctive color variation from green to yellow orange under 365 nm UV lamp as illustrated in the Figure 3.22. Furthermore, paper based fluorescent test strips were prepared to confirm its potential use for the RhB detection. The CPB@ZIF-8 coated filter test paper (∼1 cm × 1 cm) displayed a green color under UV lamp of 365 nm wavelength. When 20 ppm RhB solution was applied to the coated test paper, a sharp transition from green to yellow was noticed. These findings demonstrate the potential of the paper sensor for on-spot detection of RhB.

Figure 3.22: Images taken with a 365 nm UV lamp of the CPB@ZIF-8 dispersed solution (a) and coated test paper with increasing concentrations of RhB dye.

(c) Selectivity investigation

Selectivity test of the sensor towards rhodamine blue dye was carried out in presence of different dye solution (e.g., alizarin red, congo red, malachite green, methyl orange, crystal violet, allura red, and mixture of all the dye solution). The ratiometric PL response was observed only with rhodamine blue indicating the selectivity of the sensing probe for rhodamine blue (Figure 3.23).

3.3.6.3. Validation of the proposed sensor using real samples

The real sample analysis of 4-nitroaniline has been performed with soil sample and tap water sample by the synthesized sensor. A known concentration of analyte is first added to the real samples and then tested the spiked sample and determines if we have recovered the amount that we added. 13.8 mg of 4-NA were first added to 2.0 g of soil sample and mixed the content using a mortar pestle.
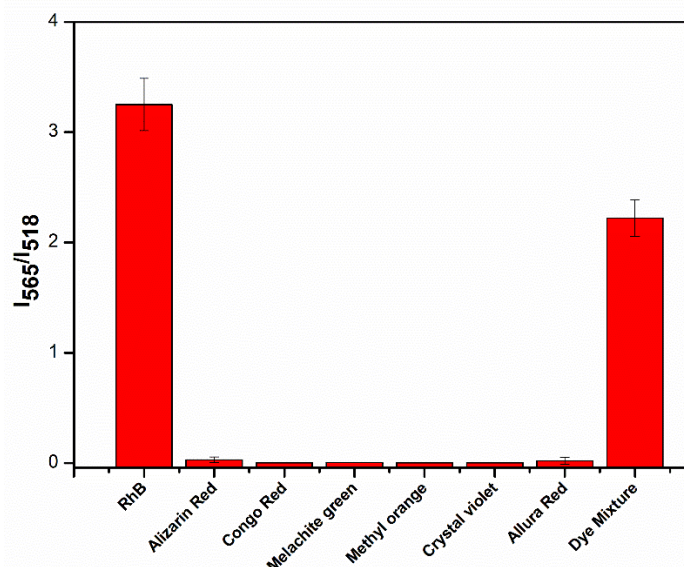
Figure 3.23: Selectivity of the CPB@ZIF-8 sensing probe towards RhB dye.

Then, 100 mL of methanol was added and ultrasonicate the mixture for 30 min. Following the centrifugation of the mixture for 5 min at 5000 rpm, supernatant was collected which was then diluted to prepare different known concentration of 4-NA. Then 4 ml of CPB@ZIF-8 dispersion was mixed with the prepared soil samples and fluorescence measurements were performed. Similarly different known concentrations (0, 0.5, 5 and 10 μM) of 4-NA were added to tap water sample and then fluorescence measurements were carried out.

The data mentioned in the following Table 3.5 and Table 3.6 showed a recovery percentage in the range of 92-103 %, with a relative standard deviation percentage (RSD) value in between 1.8 % to 5 %. for added 4-NA in soil sample. For tap water samples the recovery percentages were found to be 101%, 100.2%, and 93.2 %. Similarly real sample analysis of the sensor for RhB was also carried out using tap water samples and food samples (Fruit juice).

Table 3.5. Summary of 4-NA analysis in real samples

Sample	Added 4-NA (μM)	Detected 4-NA (μM)	Recovery (%)	RSD % (n=3)
Soil Sample	0	Not detected	–	–
	0.5	0.465	93	5
	5	5.15	103	1.8
	20	18.4	92	4.9
Tap water sample	0	Not detected	–	–
	0.5	0.505	101	5.5
	5	5.01	100.2	2.4
	10	9.32	93.2	5.6

Table 3.6. Summary of RhB analysis in real samples

Sample	Added RhB (μM)	Detected RhB (μM)	Recovery (%)	RSD % (n=3)
Fruit Juice	0	Not detected	–	–
	5	4.15	83	6.8
	10	9.25	92.5	3.9
	15	13.4	89.3	5.15
Tap water sample	0	Not detected	–	–
	5	5.08	101.6	3.09
	10	9.48	94.8	2.33
	15	14.8	98.6	5.16

3.4. Conclusion

- ✓ An in-situ (one step) method was employed to synthesize $CsPbBr_3$ perovskite quantum dots in ZIF-8 MOF matrix.

- ✓ The resulting composite exhibited stable, highly intense, and narrow emission centered at 518 nm with FWHM of 20 nm.

- ✓ The designed CPB@ZIF-8 composite showed quenching of PL signal in presence of nitroaromatic compounds and selectively and quickly detect 4-nitro aniline with a LOD value of 8.367 ppb. Also, it can differentiate nitroaniline isomers through FL sensing.

- ✓ The same CPB@ZIF-8 composite acted as ratiometric FL probe for rhodamine blue dye and LOD was calculated to be 0.088 ppm.

- ✓ Paper based sensor on filter paper was fabricated for visual on spot detection of both the analytes.

- ✓ The applicability of this sensor was demonstrated by applying it to the real sample analysis.

3.5. References

[1]   Wu, P., Liu, Y., Li, Y., Jiang, M., Li, X. L., Shi, Y., and Wang, J. A cadmium (ii)-based metal–organic framework for selective trace detection of nitroaniline isomers and photocatalytic degradation of methylene blue in neutral aqueous solution. *Journal of Materials Chemistry A*, 4(42):16349-16355, 2016.

[2]   Deshmukh, A., Bandyopadhyay, S., James, A., and Patra, A. Trace level detection of nitroanilines using a solution processable fluorescent porous organic polymer. *Journal of Materials Chemistry C*, 4(20):4427-4433, 2016.

[3]   Yang, Y. J., Wang, M. J., and Zhang, K. L. A novel photoluminescent Cd (II)–organic framework exhibiting rapid and efficient multi-responsive fluorescence sensing for trace amounts of Fe^{3+} ions and some NACs, especially for 4-nitroaniline and 2-methyl-4-nitroaniline. *Journal of Materials Chemistry C*, 4(48):11404-11418, 2016.

[4]   Wu, D., Zhou, K., Tian, J., Liu, C., Jiang, F., Yuan, D., Chen, Q., and Hong, M. A tubular luminescent framework: precise decoding of nitroaniline isomers and

quantitative detection of traces of benzaldehyde in benzyl alcohol. *Journal of Materials Chemistry C*, 8(29):9828-9835, 2020.

[5] Wei, F., Cai, X., Nie, J., Wang, F., Lu, C., Yang, G., Chen, Z., Ma, C., and Zhang, Y. A 1, 2, 3-triazolyl based conjugated microporous polymer for sensitive detection of p-nitroaniline and Au nanoparticle immobilization. *Polymer Chemistry*, 9(27): 3832-3839, 2018.

[6] Lu, X., Yang, Y., Zeng, Y., Li, L., and Wu, X. Rapid and reliable determination of p-nitroaniline in wastewater by molecularly imprinted fluorescent polymeric ionic liquid microspheres. *Biosensors and Bioelectronics*, 99:47-55, 2018.

[7] Yang, J., Xia, L., Lin, Z., Tang, Z., Li, G., and Hu, Y. Core (Au)-shell (Ag) structure nitrogen dots for the recognition of nitroaniline isomers by surface-enhanced Raman scattering. *Chinese Chemical Letters*, 30(3):638-642, 2019.

[8] Wang, S. P. and Chen, H. J. Separation and determination of nitrobenzenes by micellar electrokinetic chromatography and high-performance liquid chromatography. *Journal of Chromatography A*, 979(1-2):439-446, 2002.

[9] Tropp, J., Ihde, M. H., Crater, E. R., Bell, N. C., Bhatta, R., Johnson, I. C., Bonizzoni, M., and Azoulay, J. D. A sensor array for the nanomolar detection of azo dyes in water. *ACS sensors*, 5(6):1541-1547, 2020.

[10] Sun, Y., Li, W., Zhao, L., Li, F., Xie, Y., Yao, W., Liu, W., and Lin, Z. Simultaneous SERS detection of illegal food additives rhodamine B and basic orange II based on Au nanorod-incorporated melamine foam. *Food Chemistry*, 357:129741, 2021.

[11] Singh, A., Qu, Z., Sharma, A., Singh, M., Tse, B., Ostrikov, K., Popat, A., Sonar, P., and Kumeria, T. Ultra-bright green carbon dots with excitation-independent fluorescence for bioimaging. *Journal of Nanostructure in Chemistry*, 13(3):377-387, 2023.

[12] Guan, J., Shen, Y. Z., Shu, Y., Jin, D., Xu, Q., and Hu, X. Y. Internal–External Stabilization Strategies Enable Ultrastable and Highly Luminescent CsPbBr3 Perovskite Nanocrystals for Aqueous Fe3+ Detection and Information Encryption. *Advanced Materials Interfaces*, 8(19):2100588, 2021.

[13] Halali, V. V., Sanjayan, C. G., Suvina, V., Sakar, M., and Balakrishna, R. G. Perovskite nanomaterials as optical and electrochemical sensors. *Inorganic Chemistry Frontiers*, 7(14):2702-2725, 2020.

[14] Resch-Genger, U., Grabolle, M., Cavaliere-Jaricot, S., Nitschke, R., and Nann, T. Quantum dots versus organic dyes as fluorescent labels. *Nature methods*, 5(9):763-775, 2008.

[15] Silvi, S. and Credi, A. Luminescent sensors based on quantum dot–molecule conjugates. *Chemical Society Reviews*, 44(13):4275-4289, 2015.

[16] Zhang, H., Wang, X., Liao, Q., Xu, Z., Li, H., Zheng, L., and Fu, H. Embedding perovskite nanocrystals into a polymer matrix for tunable luminescence probes in cell imaging. *Advanced Functional Materials*, 27(7):1604382, 2017.

[17] Sheng, X., Liu, Y., Wang, Y., Li, Y., Wang, X., Wang, X., Dai, Z., Bao, J., and Xu, X. Cesium lead halide perovskite quantum dots as a photoluminescence probe for metal ions. *Advanced Materials*, 29(37):1700150, 2017.

[18] Zhao, Y., Xu, Y., Shi, L., and Fan, Y. Perovskite nanomaterial-engineered multiplex-mode fluorescence sensing of edible oil quality. *Analytical chemistry*, 93(31):11033-11042, 2021.

[19] Chen, X., Hu, H., Xia, Z., Gao, W., Gou, W., Qu, Y., and Ma, Y. CsPbBr$_3$ perovskite nanocrystals as highly selective and sensitive spectrochemical probes for gaseous HCl detection. *Journal of Materials Chemistry C*, 5(2):309-313, 2017.

[20] Xiang, X., Ouyang, H., Li, J., and Fu, Z. Humidity-sensitive CsPbBr$_3$ perovskite based photoluminescent sensor for detecting Water content in herbal medicines. *Sensors and Actuators B: Chemical*, 346:130547, 2021.

[21] Huangfu, C. and Feng, L. High-performance fluorescent sensor based on CsPbBr3 quantum dots for rapid analysis of total polar materials in edible oils. *Sensors and Actuators B: Chemical*, 344:130193, 2021.

[22] Chen, X., Sun, C., Liu, Y., Yu, L., Zhang, K., Asiri, A. M., Marwani, H. M., Tan, H., Ai, Y., Wang, X. and Wang, S. All-inorganic perovskite quantum dots CsPbX3 (Br/I) for highly sensitive and selective detection of explosive picric acid. *Chemical Engineering Journal*, 379:122360, 2020.

[23] Cravillon, J., Nayuk, R., Springer, S., Feldhoff, A., Huber, K., and Wiebcke, M. Controlling zeolitic imidazolate framework nano-and microcrystal formation: insight into crystal growth by time-resolved in situ static light scattering. *Chemistry of Materials*, 23(8):2130-2141, 2011.

[24] Abuzalat, O., Wong, D., Park, S. S., and Kim, S. Highly selective and sensitive fluorescent zeolitic imidazole frameworks sensor for nitroaromatic explosive detection. *Nanoscale*, 12(25):13523-13530, 2020.

[25] Hou, J., Wang, Z., Chen, P., Chen, V., Cheetham, A. K., and Wang, L. Intermarriage of halide perovskites and metal-organic framework crystals. *Angewandte Chemie*, 132(44):19602-19617, 2020.

[26] Abdelhamid, H. N., Huang, Z., El-Zohry, A. M., Zheng, H., and Zou, X. A fast and scalable approach for synthesis of hierarchical porous zeolitic imidazolate frameworks and one-pot encapsulation of target molecules. *Inorganic chemistry*, 56(15):9139-9146, 2017.

[27] Morris, W., Stevens, C. J., Taylor, R. E., Dybowski, C., Yaghi, O. M., & Garcia-Garibay, M. A. (2012). NMR and X-ray study revealing the rigidity of zeolitic imidazolate frameworks. *The Journal of Physical Chemistry C*, *116*(24), 13307-13312.

[28] Ren, J., Li, T., Zhou, X., Dong, X., Shorokhov, A. V., Semenov, M. B., Krevchik, V. D., and Wang, Y. Encapsulating all-inorganic perovskite quantum dots into mesoporous metal organic frameworks with significantly enhanced stability for optoelectronic applications. *Chemical Engineering Journal*, 358:30-39, 2019.

[29] Kong, Z. C., Liao, J. F., Dong, Y. J., Xu, Y. F., Chen, H. Y., Kuang, D. B., and Su, C. Y. Core@ shell CsPbBr3@ zeolitic imidazolate framework nanocomposite for efficient photocatalytic CO2 reduction. *ACS Energy Letters*, 3(11):2656-2662, 2018.

[30] Nandi, N., Sarkar, P., and Sahu, K. N-doped carbon dots for visual recognition of 4-nitroaniline and use in fluorescent inks. *ACS Applied Nano Materials*, 4(9):9616-9624, 2021.

[31] Ji, N. N., Shi, Z. Q., Hu, H. L., and Zheng, H. G. A triphenylamine-functionalized luminescent sensor for efficient p-nitroaniline detection. *Dalton Transactions*, 47(21):7222-7228, 2018.

[32] Yuan, H., Li, D., Liu, Y., Xu, X., and Xiong, C. Nitrogen-doped carbon dots from plant cytoplasm as selective and sensitive fluorescent probes for detecting p-nitroaniline in both aqueous and soil systems. *Analyst*, 140(5):1428-1431, 2015.

[33] Shan, X., Zhang, S., Zhou, M., Geske, T., Davis, M., Hao, A., Wang, H., and Yu, Z. Porous halide perovskite–polymer nanocomposites for explosive detection with a high sensitivity. *Advanced Materials Interfaces*, 6(3):801686, 2019.

[34] Huang, S., Guo, M., Tan, J., Geng, Y., Wu, J., Tang, Y., Su, C., Lin, C. C., and Liang, Y. Novel fluorescence sensor based on all-inorganic perovskite quantum dots coated with molecularly imprinted polymers for highly selective and sensitive detection of omethoate. *ACS applied materials & interfaces*, 10(45):39056-39063, 2018.

[35] Ock, K. S., Ganbold, E. O., Jeong, S., Seo, J. H., and Joo, S. W. CdS nanoparticles as efficient fluorescence resonance energy transfer donors for various organic dyes in an aqueous solution. *Bull. Korean Chem. Soc*, 32(10):3611, 2011.

[36] Li, Y., He, W., Peng, Q., Hou, L., He, J., and Li, K. Aggregation-induced emission luminogen based molecularly imprinted ratiometric fluorescence sensor for the detection of Rhodamine 6G in food samples. *Food chemistry*, 287:55-60, 2019.

[37] Wang, Y., Zhu, Y., Huang, J., Cai, J., Zhu, J., Yang, X., Shen, J., Jiang, Hao., and Li, C. CsPbBr3 perovskite quantum dots-based monolithic electrospun fiber membrane as an ultrastable and ultrasensitive fluorescent sensor in aqueous medium. *The journal of physical chemistry letters*, 7(21):4253-4258, 2016.

[38] Li, Y., Hou, L., Shan, F., Zhang, Z., Li, Y., Liu, Y., Peng, Q., He, J., and Li, K. A novel aggregation-induced emission luminogen based molecularly imprinted fluorescence sensor for ratiometric determination of Rhodamine B in food samples. *ChemistrySelect*, 4(38):11256-11261, 2019.

[39] Goedhart, J., Vermeer, J. E., Adjobo-Hermans, M. J., van Weeren, L., and Gadella Jr, T. W. Sensitive detection of p65 homodimers using red-shifted and fluorescent protein-based FRET couples. *PLoS One*, 2(10):1011, 2007.

[40] Tan, H., Wu, X., Weng, Y., Lu, Y., and Huang, Z. Z. Self-assembled FRET nanoprobe with metal–organic framework as a scaffold for ratiometric detection of hypochlorous acid. *Analytical chemistry*, 92(4):3447-3454, 2020.